

ENERGETIC IMPACT OF JET-INFLATED COCOONS IN RELAXED GALAXY CLUSTERS

JOHN C. VERNALEO AND CHRISTOPHER S. REYNOLDS

Department of Astronomy, University of Maryland, College Park, MD 20742-2421; vernaleo@astro.umd.edu, chris@astro.umd.edu

Received 2007 May 31; accepted 2007 August 29

ABSTRACT

Jets from active galactic nuclei (AGNs) in the cores of galaxy clusters have the potential to be a major contributor to the energy budget of the intracluster medium (ICM). To study the dependence of the interaction between the AGN jets and the ICM on the parameters of the jets themselves, we present a parameter survey of two-dimensional (axisymmetric) ideal hydrodynamic models of back-to-back jets injected into a cluster atmosphere (with varying Mach numbers and kinetic luminosities). We follow the passive evolution of the resulting structures for several times longer than the active lifetime of the jet. The simulations fall into roughly two classes, cocoon-bounded and non-cocoon bounded sources. We suggest a correspondence between these two classes and the Faranoff-Riley types. We find that the cocoon-bounded sources inject significantly more entropy into the core regions of the ICM atmosphere, even though the efficiency with which energy is thermalized is independent of the morphological class. In all cases, a large fraction (50%–80%) of the energy injected by the jet ends up as gravitational potential energy due to the expansion of the atmosphere.

Subject headings: cooling flows — galaxies: active — galaxies: jets — hydrodynamics — X-rays: galaxies: clusters

1. INTRODUCTION

Jets from powerful active galactic nuclei (AGNs) play a major role in shaping their environment on both the large and small scales. In many clusters of galaxies, the intracluster medium (ICM) bears the marks of repeated episodes of AGN jet activity, e.g., bubbles (Fabian et al. 2000; McNamara et al. 2000; Blanton et al. 2001; Young et al. 2002), ghost bubbles (McNamara et al. 2001; Heinz et al. 2002; Choi et al. 2004; Fabian et al. 2000), ripples (Fabian et al. 2003, 2005), shells (Fabian et al. 2000), and filaments. Besides affecting the gross morphology of the ICM, AGNs have the potential to dramatically alter the energy and entropy budgets of the ICM. This is especially of interest in relation to the cooling flow problem of galaxy clusters (Cowie & Binney 1977; Fabian & Nulsen 1977; Fabian 1994). In this paper, we attempt to determine the relationship between the jet parameters (Mach number and kinetic luminosity) and the resulting energetics and structures in the ICM.

X-ray observations show that the ICM radiates strongly in the X-ray wavelengths due to thermal bremsstrahlung radiation. In the central regions of rich, relaxed clusters, the ICM has a cooling time shorter than the Hubble time (sometimes as low as a few $\times 10^8$ yr). With such short cooling times, we would expect to see large quantities of cool gas and/or star formation in the center of rich clusters. Equivalently, the cD galaxy at the center of the cluster would be accreting cooled matter from the cooling ICM. The density-squared dependence of the emission ensures that, if this simple picture were correct, the cooling would increase and eventually reach a cooling catastrophe in a finite time.

Observations strongly suggest that large quantities of cooled gas are not being deposited in the central galaxy. The observed star formation rates in the central cD galaxies are not sufficient to match the inferred cooling rates (O’Dea et al. 2004; Hicks & Mushotzky 2005). Furthermore, the mass function of galaxies shows a high-mass truncation that argues against the continued ICM accretion growth of cD galaxies and requires a feedback process significantly more efficient than star formation (see Benson et al. 2003). More directly, high-resolution X-ray spectroscopy

with the Reflection Grating Spectrometer (RGS) on *XMM-Newton* shows that the ICM cools from the virial temperature to approximately one-third of the virial temperature but reveals an absence of plasma below this temperature. The apparent contradiction between the absence of cool gas and the short cooling times of the ICM core is the cooling flow problem (Fabian 1994).

These observational results suggest that some form of ICM heating is required to offset the radiative cooling. Intermittent activity by a central AGN remains an attractive solution. A large amount of theoretical work has been performed on the possible effects of AGNs on cooling cluster cores. With ever-increasing computer power, most of the recent work has focused on hydrodynamic models of the AGN/ICM interaction (Clarke et al. 1997; Churazov et al. 2001; Brüggén & Kaiser 2001, 2002; Reynolds et al. 2002; Basson & Alexander 2003; Omma et al. 2004; Omma & Binney 2004; Dalla Vecchia et al. 2004; Robinson et al. 2004; Zanni et al. 2005). Some groups have also begun initial explorations of the effects of magnetic fields (Robinson et al. 2004; Jones & De Young 2005), plasma processes (Ruszkowski et al. 2004; Reynolds et al. 2005), feedback prescriptions (Vernaleo & Reynolds 2006), and realistic (cosmological) background motions (Heinz et al. 2006).

Collectively, this body of simulation work has allowed us to explain many of the observed features of AGN/ICM interactions, investigate how AGN-induced flows mix metals within the ICM core, and study entropy injection and heating of the ICM. However, most of the current sets of simulation are performed for a limited set of jet parameters, and hence it is unclear how to generalize the results to the population of as a whole. In this paper, we present a moderately large set of (axisymmetric) high-resolution hydrodynamic simulations of jet/ICM interactions that survey a wide range of jet powers and jet velocities. We study the morphology of the radio galaxy as well as the injection of energy and entropy into the ICM as a function of the jet properties. In § 2, we discuss the details of our setup and the code used. In § 3, we present the analysis of our simulations and their classifications. In § 4 we discuss the results, followed by conclusions in § 5.

2. SIMULATION SETUP

Our goal is to model a relaxed cluster and its interaction with a central radio galaxy that produces back-to-back jets. To do this, we start out with an initial cluster that is both spherically symmetric and isothermal, with the (adiabatic) sound speed $c_s = 1$ everywhere. The initial cluster gas is assumed to follow a β -model density profile,

$$\rho(r) = \frac{1}{\left[1 + (r/r_0)^2\right]^{3/4}}, \quad (1)$$

where the core radius is $r_0 = 2.0$ in code units.

A static gravitational potential,

$$\Phi = \frac{c_s^2}{\gamma} \ln(\rho), \quad (2)$$

is set to make the gas initially in hydrostatic equilibrium and is assumed to remain fixed in time. This is equivalent to a potential set entirely by stationary dark matter that dominates the system, so the self-gravity of the gas is ignored. The intracluster gas, while containing a large fraction of the baryons in the cluster, is indeed not a significant contributor to the overall cluster mass.

We use spherical polar coordinates (r, θ, ϕ) and impose symmetry in the ϕ direction ($\partial/\partial\phi = 0$). The radial coordinate varied between 0.1 and 30.0 in scaled code units. The comparison between code units and physical units is given in § 2.2. The values of θ were allowed to vary between 0 and π (i.e., we are modeling the full sphere). Since we have the full range of angles, this allows us to have back-to-back jets. Thus, we can model interaction between the backflows from the jets rather than the commonly employed technique of imposing reflecting boundary conditions on the $\theta = \pi/2$ plane (e.g., see Sternberg et al. 2007; Vignelli & Reynolds 2006). We included second-order differences in grid spacing in the θ direction for each hemisphere, giving us two realizations of the jet/cocoon structure per simulation. In no cases were there major differences between the two sides, confirming that the details of the gridding do not affect our results. A small circle around $r = 0$ was excluded from the computational domain to avoid the coordinate singularity.

All simulations were run with a $n_r \times n_\theta = 1200 \times 600$ grid. In the radial direction, a ratioed grid was used, with successive cells increasing by a factor of 1.003. The θ direction also used a ratioed grid increasing by a factor of 0.998 from 0 to 0.5π and then decreasing by a factor of 1.002 from 0.5π to π . This provides the greatest number of zones near the center and near the two jet axes while providing the second-order differences in the θ direction mentioned above.

Clearly jets are three-dimensional structures. However, there is a long history of two-dimensional modeling of jets that supports the usefulness of two-dimensional jets (Carvalho & O’Dea 2002; Churazov et al. 2001; Mizuta et al. 2001; Reynolds et al. 2002). There are, however, several aspects of the dynamics that cannot be captured in two dimensions. There is no way to have realistic random motions in the background. This lack of random motions produces lobes that are far more regular and symmetric than those found in any real source. The two-dimensional assumption also enhances mixing between the high-entropy material and ambient material. This is because nonaxisymmetric Kelvin-Helmholtz (KH) and Rayleigh-Taylor (RT) modes are clearly not possible in an axisymmetric system. Without non-axisymmetric modes, all of the mixing must be done by the axi-

symmetric modes, which are more efficient at mixing (Reynolds et al. 2002). Fortunately, this will be most problematic only at late times when there has been enough time for significant mixing to occur.

The hydrodynamic evolution of the jet/ICM system was followed using the ZEUS-3D code (Stone & Norman 1992a, 1992b). ZEUS is a fixed-grid Eulerian code, explicit in time and second-order accurate (when using van Leer advection as we do). Artificial viscosity is used to handle shocks. All simulations were run as ideal hydrodynamic cases, neglecting magnetic fields and self-gravity. ZEUS solves the standard equations of hydrodynamics,

$$\frac{D\rho}{Dt} + \rho \nabla \cdot \mathbf{v} = 0, \quad (3)$$

$$\rho \frac{D\mathbf{v}}{Dt} = -\nabla P - \rho \nabla \Phi, \quad (4)$$

$$\rho \frac{D}{Dt} \left(\frac{e}{\rho} \right) = -P \nabla \cdot \mathbf{v} - \Lambda, \quad (5)$$

where

$$\frac{D}{Dt} \equiv \frac{\partial}{\partial t} + \mathbf{v} \cdot \nabla. \quad (6)$$

Radiative cooling, represented by the Λ -term in equation (5), is neglected in order to concentrate on the hydrodynamic evolution and the thermodynamic response of the ICM to the jets.

2.1. Modeling the Jets

Two back-to-back jets were injected into the center of the model cluster. This was achieved with an inflow boundary condition on the inner radial boundary. All the jets were highly supersonic with respect to the ambient sound speed and moderately to highly supersonic with respect to their internal sound speeds. Direct injection allows us to keep the details of jet acceleration and central engines outside of the grid, so we are able to solve the equations of hydrodynamics consistently within our computational grid.

The injected jets are initially conical with half-opening angles of 15° and are injected in pressure balance with the ICM core. The drop of internal pressure associated with subsequent jet expansion leads to external, pressure-driven recollimation and internal shocks, ultimately resulting in some new, self-consistently determined opening angle. Given these (fixed) assumptions, the properties of a given jet are parameterized by the kinetic luminosity L_{kin} and internal Mach number of the injected jet matter. These are related to the injection density ρ , pressure p , and velocity v by

$$\mathcal{M}_{\text{jet}} = \frac{v_j}{c_s} = v_j \sqrt{\frac{\rho}{\gamma(\gamma - 1)e}}, \quad (7)$$

$$L_{\text{kin}} = \frac{1}{2} \rho_j v_j^3 \pi r_{\text{in}}^2, \quad (8)$$

where r_{in} is the radius of the “injection nozzle” for the jet. The jet parameters for the base run ($L_{\text{kin}} = 26.47$ and $\mathcal{M}_{\text{jet}} = 10.55$; $\rho_j = 0.01$ and $v_j = 105.5$) are the same as the run presented in Reynolds et al. (2002).

A total of 26 models were run, where only the kinetic luminosity and/or the Mach number of the jets were varied. In two of these simulations, the jet lifetimes were also varied. The full list of simulations is given in Table 1. Internal Mach numbers in the range 3.7–21.1 and kinetic luminosity in the range 6.6–68.8

TABLE 1
PARAMETERS DEFINING THE 26 SIMULATIONS PRESENTED IN THIS PAPER

Run	Jet Active Time	L_{kin}	\mathcal{M}_{jet}	Morphology
1.....	1.0	26.47	10.55	Cocoon
2.....	1.0	52.94	21.1	Cocoon
3.....	1.0	26.43	15.89	Cocoon
4.....	1.0	26.31	7.39	Cocoon
5.....	1.0	68.97	10.46	Cocoon
6.....	1.0	23.32	10.54	Cocoon
7.....	1.0	52.94	10.55	Cocoon
8.....	0.5	26.47	10.55	Cocoon
9.....	1.5	26.47	10.55	Cocoon
10.....	1.0	8.91	6.47	Cocoon
11.....	1.0	17.91	9.48	Cocoon
12.....	1.0	19.98	15.0	Cocoon
13.....	1.0	31.09	20.02	Cocoon
14.....	1.0	13.24	21.1	Non-cocoon
15.....	1.0	13.23	10.55	Non-cocoon
16.....	1.0	26.47	21.1	Non-cocoon
17.....	1.0	6.62	10.55	Non-cocoon
18.....	1.0	9.96	8.99	Non-cocoon
19.....	1.0	21.01	13.0	Non-cocoon
20.....	1.0	30.1	18.02	Non-cocoon
21.....	1.0	24.98	19.0	Non-cocoon
22.....	1.0	52.99	5.28	Unresolved
23.....	1.0	26.44	3.71	Unresolved
24.....	1.0	26.43	5.27	Unresolved
25.....	1.0	10.05	5.01	Unresolved
26.....	1.0	12.15	6.54	Unresolved

NOTES.—Also in this table given are the (visual) morphological classification of the resulting structure, as judged at time $t = 2.0$. See text for more details.

were explored. The choice of parameters used was based on raising or lowering the Mach number and/or kinetic luminosity by a factor of 2 from one of the previous runs.

2.2. Comparison to Real Units

Throughout this paper, quantities are quoted in dimensionless code units unless explicitly stated otherwise. Since we are solving the equations of ideal hydrodynamics (eqs. [3]–[6]) with no additional physics added, there is no unique set of physical scales to our problem. Each simulation may therefore be compared to several different sets of physical scales. Following Reynolds et al. (2002), we quote two scalings for our simulations (although there is actually an entire three-parameter family of scalings). For our rich cluster scaling, we set the core radius $r_0 = 100$ kpc, meaning one code unit in r is equal to 50 kpc. Such clusters are hot, with sound speed $c_s = 1000$ km s $^{-1}$. This, along with the typical central number density $n_0 = 0.01$ cm $^{-3}$, gives a time unit of 50 Myr and a kinetic luminosity unit of $L_{\text{kin}} = 3.5 \times 10^{44}$ ergs s $^{-1}$. We can also consider a poor cluster scaling, $r_0 = 50$ kpc, $c_s = 500$ km s $^{-1}$, and $n_0 = 0.1$ cm $^{-3}$. These give a length unit of 25 kpc, a time unit of 10 Myr, and a kinetic luminosity unit of $L_{\text{kin}} = 4.4 \times 10^{42}$ ergs s $^{-1}$.

3. ANALYSIS AND RESULTS

The primary diagnostic for distinguishing injected jet material from ambient and shocked-ambient material is the specific entropy index,

$$\sigma = \frac{P}{\rho^\gamma}. \quad (9)$$

The ambient material (both undisturbed and shock heated) has a low specific entropy index (which ranges from 0.6 to 9), and the injected jet material has a specific entropy index on the order of 1000 for our base simulation (run 1). The specific entropy of injected material does vary with jet power, going from near 1 for the weakest jets to 10^7 for the most powerful. With only two ways to change entropy (increase with shocks and increase or decrease through numerical mixing), specific entropy generally provides a powerful way to distinguish injected (and shocked) material from the background gas. A cutoff of $\sigma = 10$ was set to separate jet material from ambient material. This is close to the highest ambient value, so we are not likely to artificially miss any material that should count as part of the cocoon/high-entropy material. We use the same entropy-index cutoff for all simulations to allow for direct comparisons to be made. This value was chosen to avoid counting ambient material that has the same range of values in all simulations. In the case of the weakest jets, this entropy index cutoff cannot pick out the preshocked jet material. Once the jet material passes through the terminal shock, however, it is always clearly distinguished from ambient material by a $\sigma = 10$ cutoff. For a further discussion of the entropy cutoff diagnostic, see Reynolds et al. (2002).

3.1. Morphological Classification

Based on the entropy maps, the simulations were visually placed into three classes. Simulations with a distinct, well-defined monolithic cocoon of jet-originating plasma were labeled as “cocoon-bounded sources” (or simply “cocoon sources”). We consider a cocoon to be a jet-inflated region of high-entropy material with a coherent structure that is well separated from the low-entropy background and relatively safe from mixing (until late times). Simulations that showed faint, wispy plumes of jet-originating material instead of well-defined cocoons were labeled “non-cocoon bounded sources” (“noncocoon sources”). The final group were those simulations that do not appear sufficiently resolved for an accurate classification. In the discussion below, we abbreviate the term “jet-originating material” to “jet material.”

An example of a typical cocoon source can be seen in Figure 1. Figure 2 shows a typical noncocoon source. A poorly resolved simulation can be seen in Figure 3. We also observe that it is possible to separate the cocoon bounded from the non-cocoon bounded sources by use of density contours. Figures 4 and 5 show density contours for a cocoon-bounded and non-cocoon bounded source, respectively. Simulations in the cocoon category appear to have the high-entropy jet material in a distinct region separated from the background by a solid density contour and remain that way until fairly late times. Noncocoon sources do not have such distinctions, and the jet material seems mixed in with the background even early on.

These classifications were performed at the same time for all simulations, $t = 2.0$. At this time, the structures have evolved passively for the same amount of time that they were driven by the jet. However, our classification does not appear to depend sensitively on the choice of time, although there are some limitations. In the very earliest stages of the active jet phase ($t < 0.2$ – 0.4), the jets are still pushing out from the inner boundary of the simulation (i.e., the morphology is strongly determined by the artificial aspects of the simulation) and classification is not meaningful. At late times ($t > 10$ – 15), mixing has disrupted all of our simulated sources and, again, eliminated any morphological distinction.

Using this classification, we can study how morphology depends on L_{jet} and \mathcal{M}_{jet} . Our results are shown in Figure 6. We

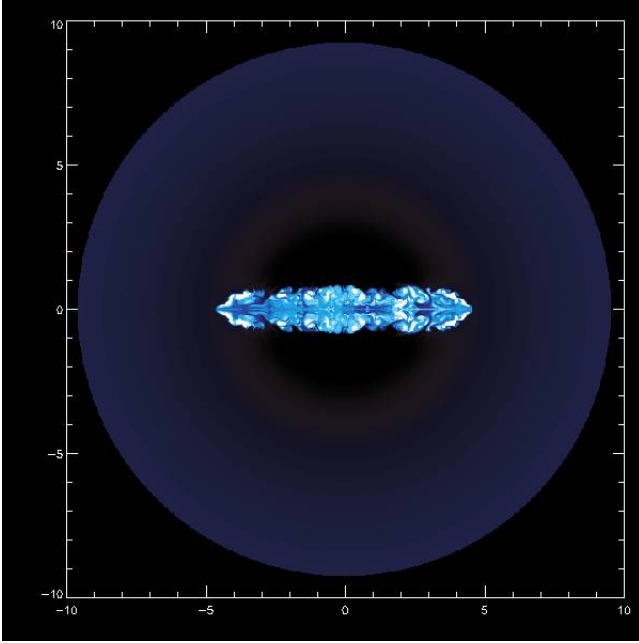


FIG. 1.—Entropy map of central regions of typical cocoon-bounded source (run 1) at $t = 2.0$.

see three separate regions on this parameter space. At the high kinetic luminosities and lower Mach numbers, the runs are unresolved. From this point on, the unresolved sources were excluded from all analysis. Low-luminosity sources seem to fall in the noncocoon category, almost regardless of Mach number (except that at high Mach number they can have a higher kinetic luminosity). The middle region contains the cocoon-bounded sources. In Figure 7, we show the parameter space again, on a density-velocity plot. Although the overlap between the morphologies is more apparent in this parameter space, we can see

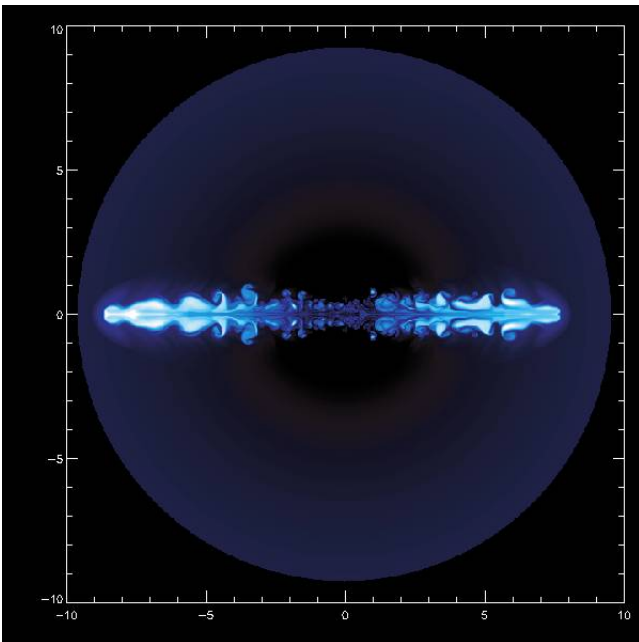


FIG. 2.—Entropy map of central regions of typical non-cocoon bounded source (run 21) $t = 2.0$.

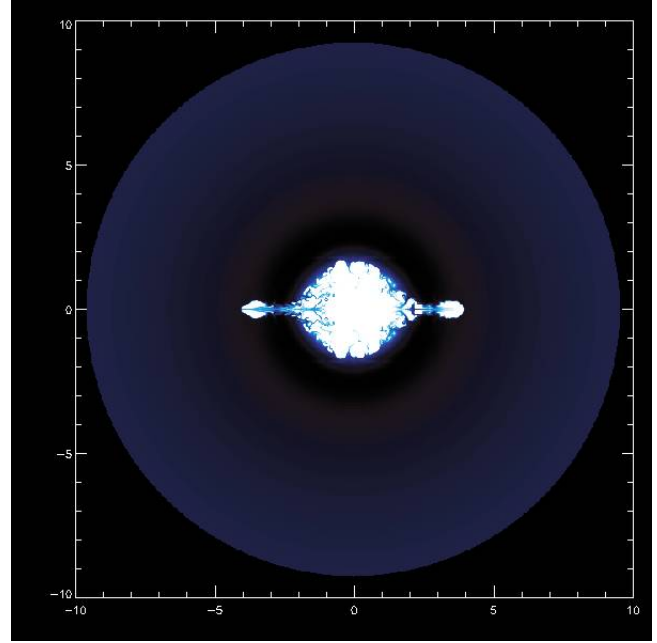


FIG. 3.—Entropy map of central regions of typical unresolved source (run 23) at $t = 2.0$.

that there appears to be a continuum of morphologies with the fastest and lightest jet producing unresolved sources at one end and the slow heavy jets producing noncocoon sources. Again, the cocoon sources occupy the middle ground between the other two. A discussion of the physical origin of the cocoon is reserved for the Discussion (§ 4).

As revealed by Figure 6, the line separating cocoon-bounded and non-cocoon bounded sources on the $(L_j, \mathcal{M}_{\text{jet}})$ plane is approximately linear (i.e., $L_j \propto \mathcal{M}_{\text{jet}}$). This can be understood from the analytic models of cocoon expansion from Begelman & Cioffi (1989). Equation (4) of Begelman & Cioffi (1989) states that the pressure of a cocoon is given by

$$p_c \sim \frac{(L_{\text{kin}} v_j \rho_a A_h)^{1/2}}{A_c}, \quad (10)$$

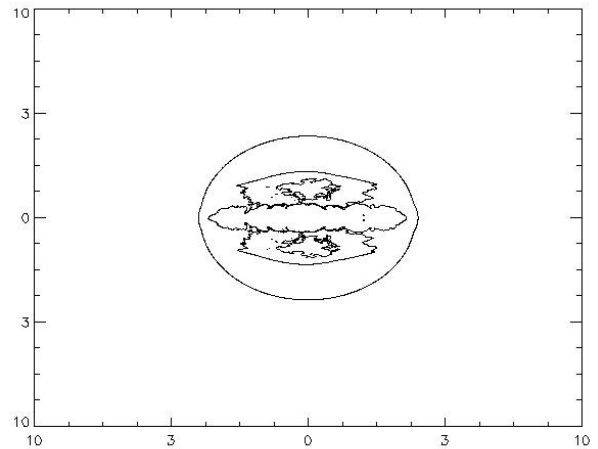


FIG. 4.—Density contours for the inner half of a cocoon-bounded source (run 1) at $t = 2.0$.

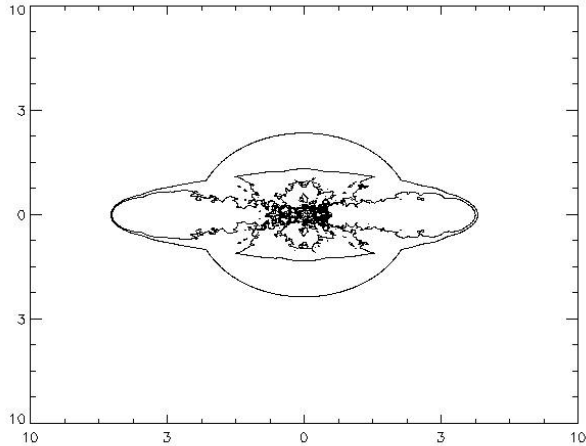


FIG. 5.—Density contours for the inner half of a non-cocoon bounded source (run 21) at $t = 2.0$.

where A_h is the area of the working surface over which the jet deposits its momentum, A_c is the cross-sectional area of the cocoon, and ρ_a is the density of the ambient ISM/ICM. Well-defined cocoons can only be sustained if p_c exceeds the pressure of the ambient medium, p_a . Noting that the axial ratio of the cocoons are approximately constant (i.e., $A_h/A_c \sim \text{constant}$), and that the density and pressure of our model ambient ICM atmosphere outside of the ICM core is the same in all simulations and drops off as $r^{-3/2}$, the condition that $p_c > p_a$ can be written as the condition

$$(L_{\text{kin}} v_j)^{1/2} > \Upsilon_{\text{crit}}, \quad (11)$$

where Υ_{crit} is a weak function of r ($\Upsilon \propto r^{1/4}$) and hence time. Since the jets are injected with fixed initial pressure, it can be shown that initial jet velocity depends on the kinetic luminosity and initial internal Mach number according to $v_j \propto L_{\text{kin}}/\mathcal{M}_{\text{jet}}^2$. Thus, we can use equation (11) to see that the line separating cocoon from noncocoon sources (i.e., where the cocoon just comes into pressure balance with the ambient ICM) can be written as $L_{\text{jet}} \propto \Upsilon \mathcal{M}_{\text{jet}}$.

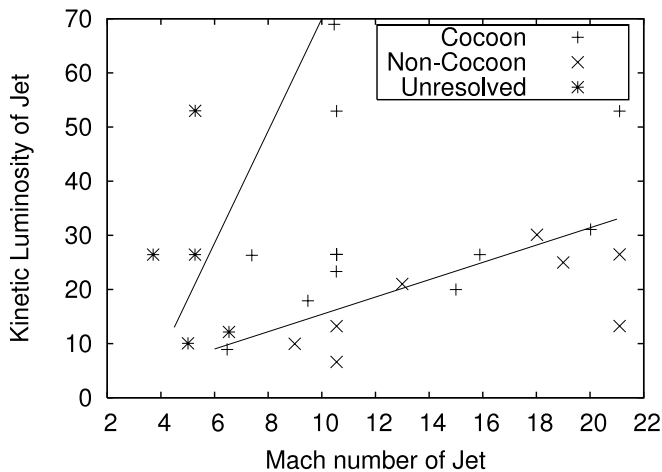


FIG. 6.—Morphology vs. jet parameters. Lines separating the different regions were done by eye. Although the lines between the different regions are not perfect, there appear to be regions in which different classes are clearly excluded.

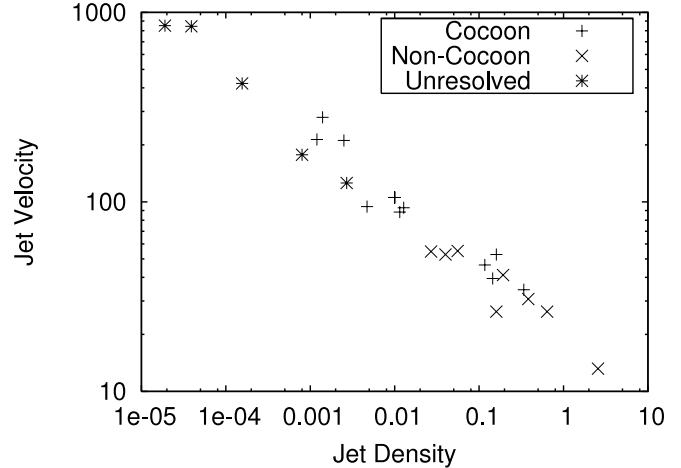


FIG. 7.—Morphology vs. jet parameters. On the density-velocity plane, we see the previously distinct regions as more of a continuum moving from one type of source to the next.

3.2. Mass Distribution and Energetics

To examine the mass distribution and energetics during the simulations, several quantities were calculated at each output time. The total mass of jet material at each time is given by

$$M_{\text{cocoon}} = \int_C \rho dV, \quad (12)$$

where C is the region with $\sigma > 10$. The internal, kinetic, and potential energies were calculated for both the jet and the ambient material,

$$E_{\text{int}}^{C,A} = \frac{1}{\gamma - 1} \int_{C,A} P dV, \quad (13)$$

$$E_{\text{kin}}^{C,A} = \frac{1}{2} \int_{C,A} \rho v^2 dV, \quad (14)$$

$$E_{\text{pot}}^{C,A} = - \int_{C,A} \rho \Phi dV. \quad (15)$$

where A is the region with $\sigma \leq 10$. In all cases, the integral is taken over only the region of interest (i.e., cocoon or ambient only, as determined by the entropy cutoff). We then subtract the initial energies in order to derive the change of energy $\Delta E_{\text{int}}^{C,A}$, $\Delta E_{\text{kin}}^{C,A}$, and $\Delta E_{\text{pot}}^{C,A}$.

The results of these calculations for a representative cocoon bounded simulation are shown in Figure 8. Figure 9 shows similar plots for a non-cocoon bounded simulation. These figures are similar to Figure 4 of Reynolds et al. (2002) and primarily differ due to our increased outer radius (and the fact that plots are continued until later times). The top left panel in each figure shows the total mass of the cocoon material compared to the amount of injected material. In both cases, this increases until the jet turns off and then begins to decrease. For the cocoon-bounded source, this decrease is mostly steady for the entire lifetime of the simulation. For the noncocoon source, the drop is much greater early on, so that about halfway through the simulation most of the high-entropy material has mixed with the background, and thus the decay rate has lessened. This enhanced mixing is a direct consequence of the lack of a well-defined contact discontinuity in the noncocoon sources. Note that the cocoon mass does not correspond to the cocoon-mass plot in Reynolds

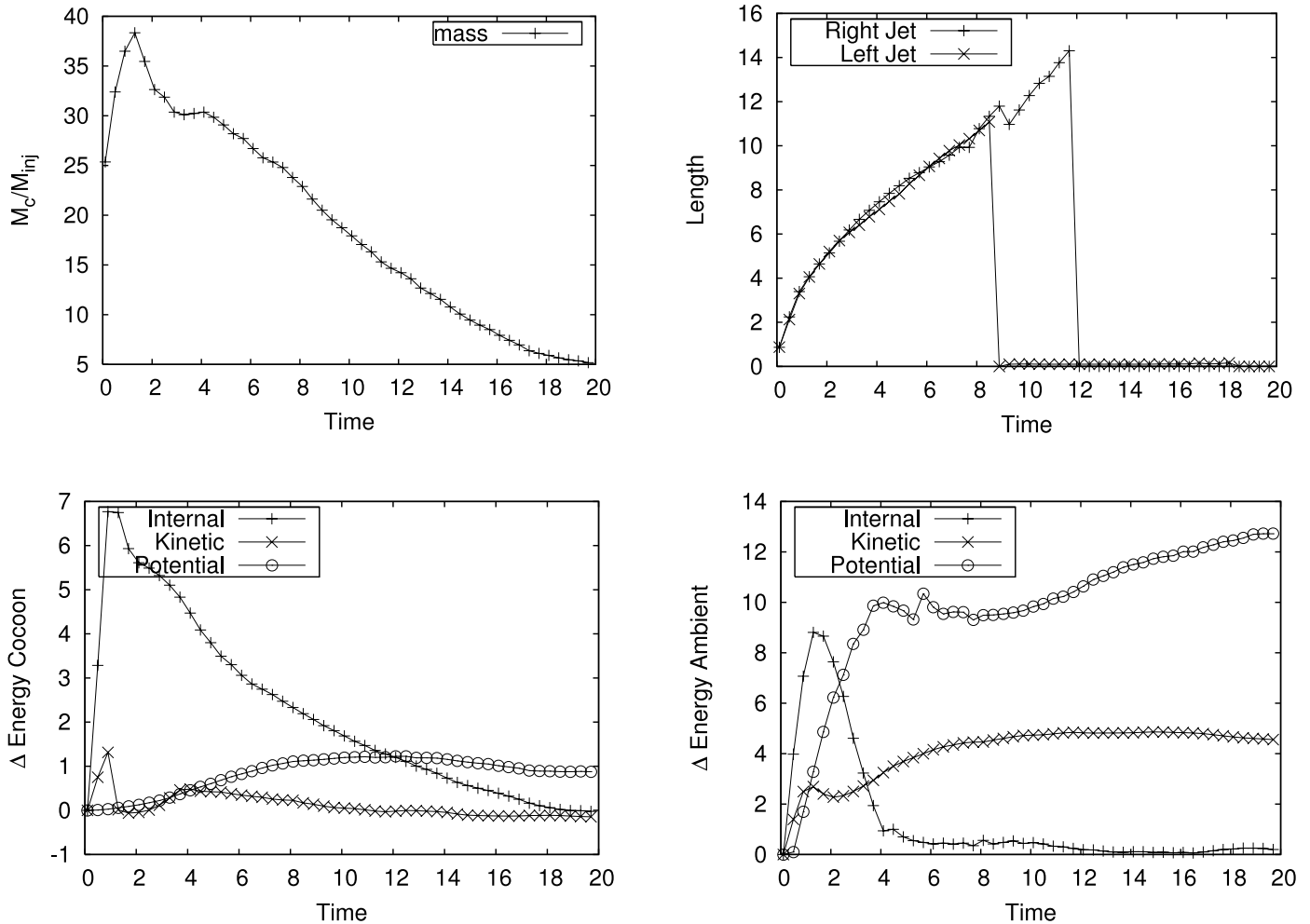


Fig. 8.—Mass and energy vs. time for a cocoon-bounded simulation (run 1). Starting from the top left and moving clockwise, the panels are: mass of the cocoon material divided by the injected mass, the maximum radial extent of the high-entropy material, the change in internal, kinetic, and potential energies for the ambient, low-entropy material compared to the initial state, and the same energy changes for the cocoon material.

et al. (2002), as we are interested in the total cocoon mass, not the change in cocoon mass.

Also shown in Figures 8 and 9 (*top right*) is the length of the region containing jet material. In the cocoon-bounded sources, the length of the cocoon evolves in a smooth manner, gradually decelerating as the cocoon comes into pressure balance with the ambient ICM. The discontinuity at late times occurs well into the phase in which the cocoon has transformed into two buoyantly rising plumes and corresponds to the complete mixing/dispersal of the leading part of the plume. The evolution of the length of the non-cocoon bounded sources, on the other hand, suffers a sharp break at the time that the jet is shut off.

Figures 8 and 9 (*bottom panels*) show the change in energies for the jet material and the ICM material, respectively. For the jet material, there is little difference in the time-dependence of the energies for the two classes, with one exception. In the non-cocoon case, the changes in internal and kinetic energy peak at a comparable value, although the kinetic drops to almost zero very soon after. For the cocoon case, the change in kinetic energy never reaches a comparable level to the change in internal energy. Physically, this is close to the heart of the difference between the cocoon and non-cocoon sources. In each case, a set amount of energy is injected by the jet (along with a set amount of mass as seen in the potential change, which is not very dramatic). The evolution of the system then determines how this

energy is split between the internal energy and the kinetic energy (and eventually how much is transferred to the ICM). In the case of the cocoon, the hot jet and shocked material is kept separate from the background and goes almost entirely into the internal energy of the shocked jet gas. For the noncocoon case, the energy is split nearly evenly between the internal and the kinetic energy. This means that there is no longer enough internal energy available to inflate a cocoon of shocked gas; more of the energy goes to the kinetic energy of the mostly bare jet (with wispy areas of hot, shocked gas around it). This is consistent with the analytic estimate of Cioffi & Blondin (1992).

The time dependence of the ICM energies show a greater difference between the two cases. The potential energy suffers a greater change (within a few times the jet lifetime) in the cocoon case due to the well-defined shell of ICM that is lifted up by the expanding cocoon, while the noncocoon case has a much more gradual change in the potential energy. The internal energy in the cocoon case drops back down to the initial value around the same time the potential peaks, while the noncocoon case has what looks like a slow trade-off between the two. Finally, the kinetic energy changes are comparable in the two cases, as there appears to be a similar amount of disturbance in the ICM regardless of the nature of the inflated structure.

In its standard configuration, ZEUS is not a strictly energy-conserving code. We do not, however, believe that this has a

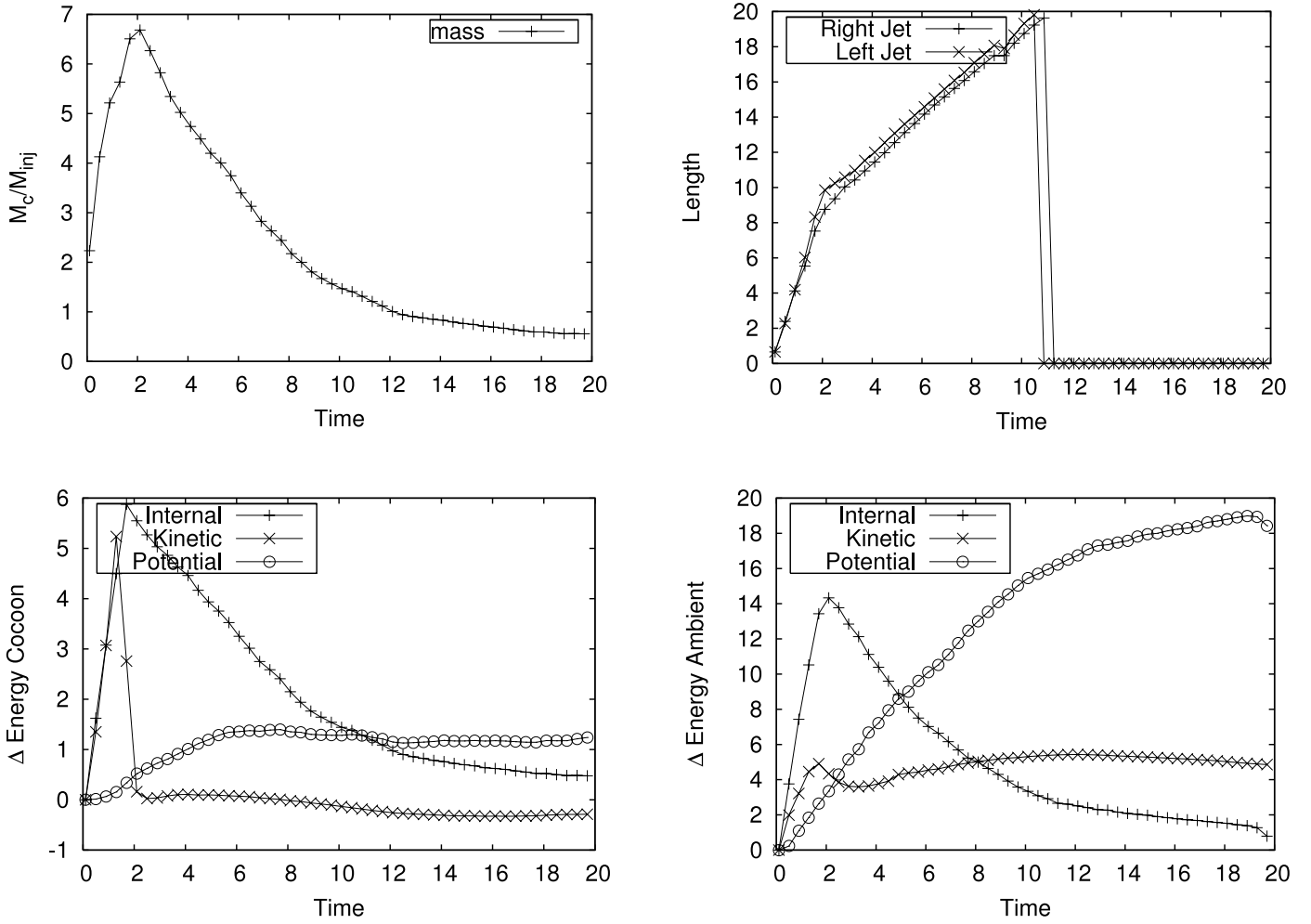


FIG. 9.—Mass and energy vs. time for a non-coocoon bounded simulation (run 21). Starting from the top left and moving clockwise, the panels are: mass of the cocoon material divided by the injected mass, the maximum radial extent of the high-entropy material, the change in internal, kinetic, and potential energies for the ambient, low-entropy material compared to the initial state, and the same energy changes for the cocoon material.

major impact on our results. Figure 10 shows that during the majority of time during the simulation, total energy is conserved to a sufficient degree. At very early times, the jet injects hot material onto the grid, which is clearly not conservative. At very late times, material (and sound waves carrying energy) leave the outer boundary of the grid. During the time in between, the energy change remains flat with only minor variations (at the 10^{-5} level), showing that energy is mostly conserved.

3.3. Entropy Evolution and Thermalization Efficiencies

We now examine the effect of the jets on the entropy of the background gas. First, we define the specific entropy,

$$\Delta S = S_1 - S_0 = \log \sigma_1 - \log \sigma_0, \quad (16)$$

where σ is the specific entropy index from equation (9).

Figure 11 shows the entropy difference (compared to the initial condition) at the final output of the simulations. At this point, the systems were allowed to evolve passively for 19 times the active lifetime of the jet. For each simulation, the total entropy at each radius was calculated and then averaged over the angular coordinate. The split between the different morphologies is evident in this figure. Within the core, the cocoon sources have a higher ΔS overall. Further discussion of this issue is reserved for § 4.

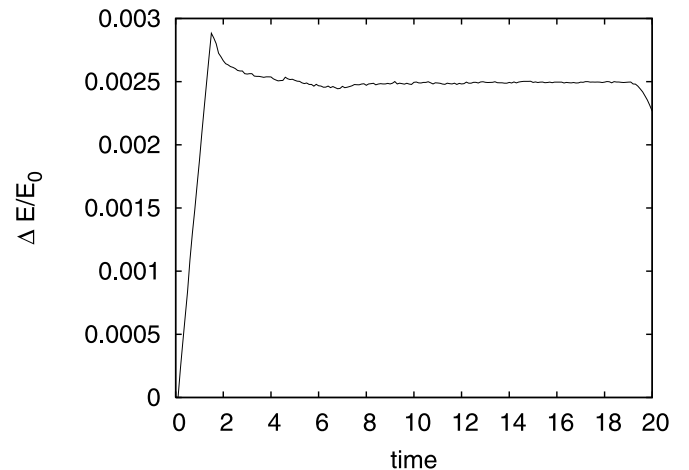


FIG. 10.—Fractional change in total energy within the simulated domain as a function of time. All forms of energy (kinetic, internal, and gravitational) for all of the gas in the computational domain are considered. Shown here is the change in total energy compared with the initial time ΔE divided by the initial total energy E_0 .

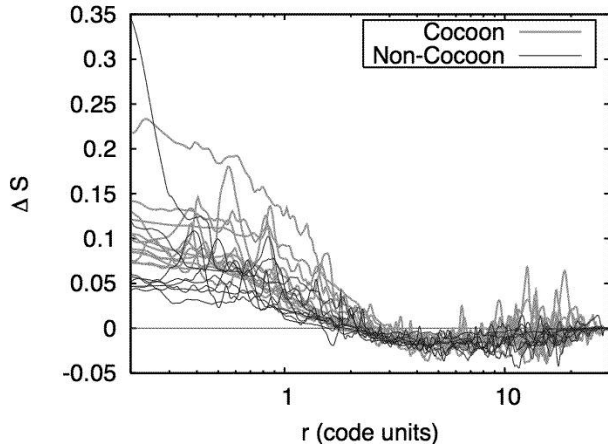


FIG. 11.—Angle-averaged change in entropy. See discussion in text for full description.

As a final look at the effect of the jets on the cluster energetics, we show the efficiencies for conversion of the injected energy into various forms within the ICM as measured at the final time for both the cocoon and noncocoon sources. This is defined as the change in each type of energy for the ICM material divided by the total amount of energy injected by the jet at the final output time of the simulation. Figures 12, 13, and 14 show the efficiency for conversion of injected energy into ICM internal energy, kinetic energy, and potential energy, respectively. There is no clear segregation between the two types although the cocoon sources do appear to cluster together somewhat. In all cases, a large fraction of the injected energy (50%–80%) ends as gravitational potential energy of the ICM as it expands in response to the AGN heating.

4. DISCUSSION

In the (resolved) simulations, we see a split in the morphology of the jet-created structures. As we saw in the parameter-space plot (Fig. 6), the presence or absence of a cocoon is not related to the jet speed or power in a simple matter. So the forms that we see do not tell us directly about the parameters of the jet that formed them. What they do tell us is something about the way the jet interacted with the ICM.

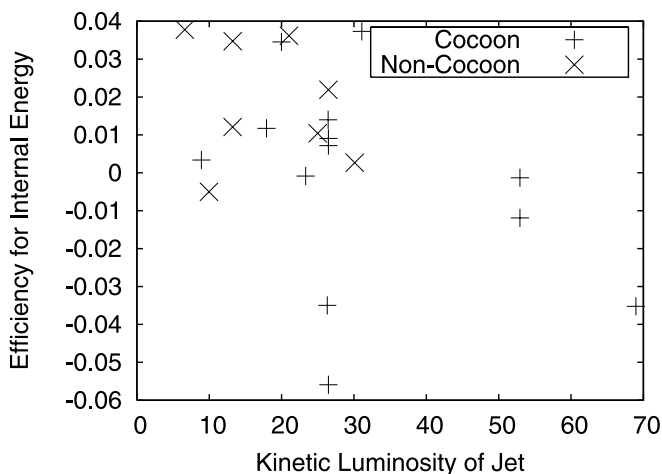


FIG. 12.—Efficiency for change in internal energy vs. kinetic luminosity for ambient medium.

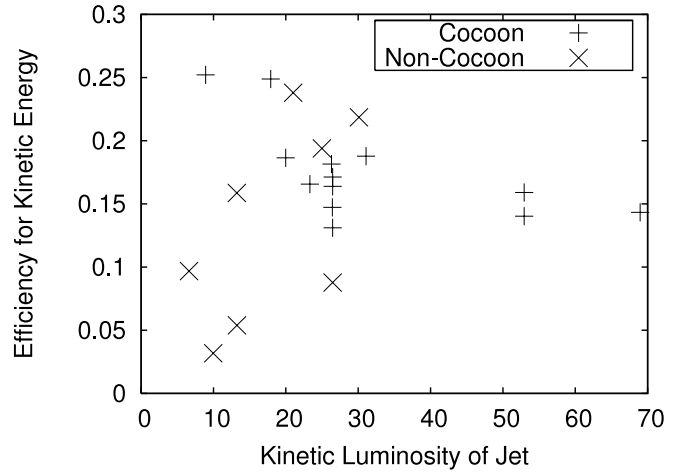


FIG. 13.—Efficiency for change in kinetic energy vs. kinetic luminosity for ambient medium.

The cocoon itself is formed by shocks. The supersonic jet initially flows freely through the ICM. After traveling some distance (usually short on the scale of these simulations), the jet will build up enough material in front of it that it can no longer flow freely. The material at the head of the jet is shock heated and expands. Up to this point, the evolution is the same for both cocoon and noncocoon sources. As this shocked material expands, the evolution diverges.

The hot, shocked material expands into the surrounding medium. At the boundaries of the shocked material, fluid instabilities (i.e., the RT and KH instabilities) work to shred the contact discontinuity and destroy the forming bubble. In the cocoon-bounded sources, the bubble is inflated before it is shredded and continues to inflate until it reaches pressure equilibrium with the background. While active, the jet deposits energy only at the point where it comes into contact with the shocked ICM, and freshly shocked material flows back from there, continuing to inflate the bubble. Once the jet ceases, the bubble floats buoyantly from the cluster center.

In the case of noncocoon sources, the jet is unable to inflate a bubble. If the jet cannot deposit enough energy at the contact point to inflate the bubble, the fluid instabilities will mix the shocked material with the background material, preventing

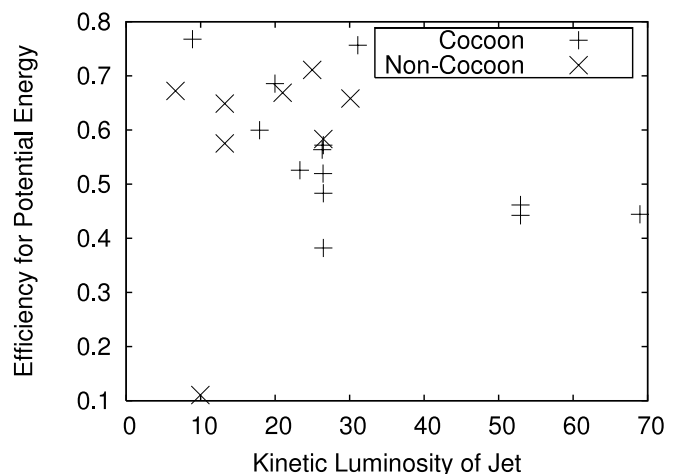


FIG. 14.—Efficiency for change in potential energy vs. kinetic luminosity for ambient medium.

the bubble from ever growing. This leaves areas of hot, shocked gas that can rise, but never produces a single coherent structure.

The clearest distinction in the thermodynamics of cocoon and noncocoon sources can be seen in the spatial distribution of the entropy enhancement. We find that in the core regions, cocoon sources cause a greater enhancement of the ICM entropy than noncocoon sources although there is some overlap. Outside the core (around $r = 5$), both appear the same and cause a slight negative change in the entropy. This negative change corresponds to lower entropy material that has been pushed upward by the expansion of the core. For the noncocoon sources, this change persists to the edge of the simulation. Some, but not all, of the cocoon sources have a spiky, positive change when approaching the edge of the grid; this corresponds to the remnants of the buoyant cocoon that, in some cases, remains intact until the end of the simulation. It is important to note that the comparison of overall entropy change was done at the final output ($t = 20$). This is long after our classifications were done. At this point, mixing has disturbed the structure enough that it would no longer be possible to separate the simulations into cocoon or noncocoon categories. The fact that we still see a difference at this late a time shows that the jets have long-lasting effects on the energetics of the ICM and that these effects vary based on the jet properties in a way that is more complicated than simply depending on jet power.

The energy efficiencies (Figs. 12, 13, and 14) are initially puzzling. The noncocoon simulations generally seem to coincide with the highest-efficiency cocoon simulations for internal and potential energy efficiency. For the kinetic energy (Fig. 13), the noncocoon runs seem to have close to both the highest values and the lowest values. This is in contrast with the situation for entropy where the cocoon simulations have a greater impact. It is fairly clear why the cocoon sources have a great entropy enhancement overall: shocks. The cocoon is formed by shocked gas, so jets that are capable of forming cocoons are also generally the ones that shock more ICM (although this is not the entire story, as the rate of shocked gas vs. mixed gas matters as well). It is not as immediately obvious why jets that are good at increasing the entropy are not always as good at increasing the energy and why there can be a spread in efficiencies for jets with similar parameters. To see why, we must go back to equation (9), the definition of the specific entropy index (keeping in mind that the pressure, P , is directly proportional to the internal energy). For a given change in internal energy, the change in entropy can be higher (or lower) by having it take place at a lower (or higher) density. So if the shocks happen higher in the potential well (and hence at a lower density), it is possible to have a greater change in entropy for the same amount of energy input. The spread in kinetic energies shows that it is possible to stir up the gas significantly with both the cocoon-producing and the non-cocoon producing jets. Also, as stated in the discussion, the cocoon-producing jets leave more energy available as internal energy, which can go toward shocks, while the non-cocoon producing jets have more of their energy in kinetic energy, which does not go to shocks and therefore is not available to increase the entropy. It is also the case that different jets will cause a different amount of material and energy to be lost from the system at the outer edge of the grid. We consider it to be reasonable to count this as lost energy as anything that has not managed to heat the gas by the time it reaches the outer edge is clearly not going to be able to change the temperature of the system.

This disconnect between entropy increase and energy increase also fits in with the results from Vernaleo & Reynolds

(2006), which showed that even with large amounts of energy available, a jet can produce large, well-formed cocoons yet fail to significantly heat the ICM. The large cocoons indicate a large change in entropy, but the central regions were still not heated significantly. This helps to reaffirm the point that in pure hydrodynamics, it is hard to energetically couple powerful jets to the *core* regions of the ICM (where it is needed to solve the cooling flow problem!).

Along with the energetic issues, we may also compare these simulations to observations in a broad sense. Classically, radio galaxies are split into two categories: Fanaroff-Riley type I (FR I) and Fanaroff-Riley type II (FR II; Fanaroff & Riley 1974). Lacking any information on luminosities and radio emission, we cannot directly compare our simulations to these classes of real radio galaxies, but we can note some interesting correlations. FR II galaxies encompass the large, back-to-back classical double-sided sources. Our cocoon-bounded sources are reminiscent of the classical doubles. The less lobe-dominated and often bent FR I sources share a similar structure with our noncocoon sources. Although our classifications were done based on the passive phase of the system, we can also compare the jets from the active phase to the FR I/FR II divide. As seen in Figures 6 and 7, slow, heavy, and lower luminosity jets (the noncocoon cases) should correspond to the FR I sources while fast, light, and more luminous jets should correspond to the FR II type. As FR II galaxies have higher luminosity jets (Ledlow & Owen 1996), this is at least consistent with our simulations. Even without a definite correspondence between the two, we do show that it is possible to produce qualitatively different structures with differences in the jet parameters without any environmental changes.

Two additional simulations (run 8 and run 9) were performed where all the parameters were kept the same as our standard case (run 1), but the active time of the jet was varied. In run 8, the jet had an active time of only $t_j = 0.5$, while run 9 had an active time of $t_j = 1.5$. In both cases, these simulations fall in the same cocoon-bounded category as run 1. This gives us some confidence that our results are not simply based on the amount of total energy injected by the jet, but instead depend on the detailed hydrodynamic interactions between the jets and the ambient material.

5. CONCLUSION

We have performed a large number of axisymmetric simulations of AGN jets in cluster atmospheres. By limiting ourselves to pure hydrodynamics with no radiative cooling, we are able to carefully study the interaction of the atmosphere with the jets and the formation of cocoons and bubbles in the cluster. With the continued interest in the probable role of jets and bubbles in the cooling flow problem, it is important that we understand their dynamics as clearly as possible.

Our main results are summarized in Figures 6 and 11. The morphology versus jet parameters plot shows that we are able to produce two distinct classes of structures, cocoon bound and non-cocoon bound, by varying the initial jet parameters. This distinction does not change with a change in total injected energy (as seen when we vary the jet lifetime) and is a function of both jet parameters (Mach number and kinetic luminosity). We can also visually draw comparisons between our two classes and the FR I and FR II distinction among real radio galaxies. The angle-averaged entropy change versus radius shows that along with the split in morphology the effect on the energetics of the ICM also depends on the jet parameters. We also see that even short-lived single-burst jets are capable of a long-lived enhancement of the entropy of a cluster core.

We would like to thank the developers of ZEUS-3D and NCSA for providing the code we used. We would like to thank the anonymous referee for useful comments that allowed us to enhance the discussion in several ways. All simulation in this

paper were performed on the Beowulf cluster (“the Borg”) in the Department of Astronomy, University of Maryland. We thank support from Chandra Theory and Modeling Program under grants TM4-5007X and TM7-8009X.

REFERENCES

- Basson, J. F., & Alexander, P. 2003, MNRAS, 339, 353
 Begelman, M. C., & Cioffi, D. F. 1989, ApJ, 345, L21
 Benson, A. J., Bower, R. G., Frenk, C. S., Lacey, C. G., Baugh, C. M., & Cole, S. 2003, ApJ, 599, 38
 Blanton, E. L., Sarazin, C. L., McNamara, B. R., & Wise, M. W. 2001, ApJ, 558, L15
 Brüggen, M., & Kaiser, C. R. 2001, MNRAS, 325, 676
 ———. 2002, Nature, 418, 301
 Carvalho, J. C., & O’Dea, C. P. 2002, ApJS, 141, 371
 Choi, Y., Reynolds, C. S., Heinz, S., Rosenberg, J. L., Perlman, E. S., & Yang, J. 2004, ApJ, 606, 185
 Churazov, E., Brüggen, M., Kaiser, C. R., Böhringer, H., & Forman, W. 2001, ApJ, 554, 261
 Cioffi, D. F., & Blondin, J. M. 1992, ApJ, 392, 458
 Clarke, D. A., Harris, D. E., & Carilli, C. L. 1997, MNRAS, 284, 981
 Cowie, L. L., & Binney, J. 1977, ApJ, 215, 723
 Dalla Vecchia, C., Bower, R. G., Theuns, T., Balogh, M. L., Mazzotta, P., & Frenk, C. S. 2004, MNRAS, 355, 995
 Fabian, A. C. 1994, ARA&A, 32, 277
 Fabian, A. C., & Nulsen, P. E. J. 1977, MNRAS, 180, 479
 Fabian, A. C., Sanders, J. S., Allen, S. W., Crawford, C. S., Iwasawa, K., Johnstone, R. M., Schmidt, R. W., & Taylor, G. B. 2003, MNRAS, 344, L43
 Fabian, A. C., Sanders, J. S., Taylor, G. B., & Allen, S. W. 2005, MNRAS, 360, L20
 Fabian, A. C., et al. 2000, MNRAS, 318, L65
 Fanaroff, B. L., & Riley, J. M. 1974, MNRAS, 167, 31P
 Heinz, S., Brüggen, M., Young, A., & Levesque, E. 2006, MNRAS, 373, L65
 Heinz, S., Choi, Y., Reynolds, C. S., & Begelman, M. C. 2002, ApJ, 569, L79
 Hicks, A. K., & Mushotzky, R. 2005, ApJ, 635, L9
 Jones, T. W., & De Young, D. S. 2005, ApJ, 624, 586
 Ledlow, M. J., & Owen, F. N. 1996, AJ, 112, 9
 McNamara, B. R., et al. 2000, ApJ, 534, L135
 ———. 2001, ApJ, 562, L149
 Mizuta, A., Yamada, S., & Takabe, H. 2001, J. Korean Astron. Soc., 34, 329
 O’Dea, C. P., Baum, S. A., Mack, J., Koekemoer, A. M., & Laor, A. 2004, ApJ, 612, 131
 Omma, H., & Binney, J. 2004, MNRAS, 350, L13
 Omma, H., Binney, J., Bryan, G., & Slyz, A. 2004, MNRAS, 348, 1105
 Reynolds, C. S., Heinz, S., & Begelman, M. C. 2002, MNRAS, 332, 271
 Reynolds, C. S., McKernan, B., Fabian, A. C., Stone, J. M., & Vignelli, J. C. 2005, MNRAS, 357, 242
 Robinson, K., et al. 2004, ApJ, 601, 621
 Ruszkowski, M., Brüggen, M., & Begelman, M. C. 2004, ApJ, 611, 158
 Sternberg, A., Pizzolato, F., & Soker, N. 2007, ApJ, 656, L5
 Stone, J. M., & Norman, M. L. 1992a, ApJS, 80, 753
 ———. 1992b, ApJS, 80, 791
 Vignelli, J. C., & Reynolds, C. S. 2006, ApJ, 645, 83
 Young, A. J., Wilson, A. S., & Mundell, C. G. 2002, ApJ, 579, 560
 Zanni, C., Murante, G., Bodo, G., Massaglia, S., Rossi, P., & Ferrari, A. 2005, A&A, 429, 399

Note added in proof.— It has been brought to our attention by Noam Soker that some of our noncocoon runs have significant mass feedback.